PERGAMON International Journal of Multiphase Flow 26 (2000) 267–292

International Journal of Multiphase Flow

www.elsevier.com/locate/ijmulflow

# Analysis of the effect of collisions on the gravitational motion of large particles in a vertical duct

S. Fohanno*, B. Oesterlé

*Laboratoire Universitaire de Mécanique et d'Energétique de Nancy (LUMEN), ESSTIN, Université Henri Poincaré, Nancy 1, Rue Jean Lamour, F-54500 Vandoeuvre-lès-Nancy, France*

Received 31 July 1998; received in revised form 7 January 1999

## Abstract

Experimental and numerical investigations of the gravitational motion of large particles in a vertical duct have been carried out in order to improve the knowledge of particle-to-particle collision effects in gas–solid confined flows. An experimental facility, consisting of a collisional flow of large spherical glass particles (3 mm in diameter) in a vertical convergent channel has been set up. Particle flow characteristics were investigated by means of a photographic technique of visualization combined with image analysis. Experiments have been performed with two particle mass flow rates corresponding to solid volume fractions of $6.5 \times 10^{-4}$ and $1.9 \times 10^{-3}$. A significant effect of the collisions between particles upon the evolution of some of the characteristics of the flow has been experimentally shown. Particle–wall collision properties have also been measured in order to provide coefficients of the collision model used in a three-dimensional Monte Carlo type Lagrangian simulation code. Particle-to-particle collisions have been taken into account by means of the probabilistic collision model. The comparison of measurements with predictions of the Lagrangian simulation code showed the suitability of the probabilistic collision model. However, the necessity for a better knowledge of particle-to-particle collision frequency, as also for an accurate knowledge of particle–wall collision properties, is pointed out. Non-negligible effects of spin-induced forces on large particles have also been observed. © 2000 Elsevier Science Ltd. All rights reserved.

*Keywords:* Two-phase flow; Gas–solid flow; Experimental study; Lagrangian simulation; Particle collisions

---

* Corresponding author.

PII: S0301-9322(99)00005-1

## 1. Introduction

Studies of confined gas–solid flows are of practical interest in many industrial applications such as pneumatic conveying or fluidized beds. In such flows, the particle–wall interactions play a significant role on the characteristics of the dispersed phase motion for any solid phase concentration. At sufficiently high concentration, the effect of collisions between particles is no longer negligible (Crowe, 1981) even at particle volume fractions as low as $4 \times 10^{-4}$ (Tanaka and Tsuji, 1991). In order to improve the knowledge of such collisional flows, many numerical studies have been carried out during last decades, which either use an Eulerian approach where each phase is considered as a continuum fluid, or a Lagrangian approach where representative particle trajectories are computed. Early Lagrangian calculations dealt with dilute flows (for example Matsumoto and Saito, 1970a, 1970b) where only particle–wall interactions were considered. Thanks to the continuous and rapid growth of computer capacities, Lagrangian simulations of more complex flow with consideration of particle-to-particle collisions have become possible. In this case, two methods can be used to account for interparticle collisions. The first one consists in simultaneously computing the trajectories of all the particles present in the flow domain, thus making it possible to handle the collisions in a deterministic way (Ottjes, 1978; Tsuji et al., 1990; Tanaka and Tsuji, 1991). However, due to the huge number of particles in actual flows, this method is limited by present computer capacities if one wants to preserve reasonable computation time. More recently, a second method has been proposed by several authors (Oesterlé and Petitjean, 1991, 1993; Tanaka et al., 1991). It is based on a Monte Carlo type Lagrangian simulation technique, which allows the computation of only a restricted number of trajectories, in taking the particle-to-particle collisions into account by means of a probabilistic collision model. However, such probabilistic models need to be tested (Sommerfeld, 1994) by carrying out measurements on a suspension flow where collisions between particles play an important role. This is the goal of the present study, which aims at bringing an experimental contribution to the knowledge of the behaviour of large particles in a particular flow configuration where the effects of interparticle collisions are prevalent.

In the present work, an original experimental facility, mainly consisting of a vertical convergent channel, has been conceived to create a collisional flow. A photographic technique of visualization, combined with image analysis, was developed to investigate some properties of the resulting flow, such as velocities and concentration profiles of the particulate phase, and measurements have been performed by means of this technique in a flow of spherical glass particles with diameter 3 mm. Experimental data, which are presented for two solid mass flow rates, show a significant effect of collisions between particles upon the evolution of some of the characteristics of the particle flow. Particle–wall collision properties in the particular case of the vertical flow under study have also been experimentally investigated. Results of this investigation served to provide values for the coefficients of the impact model used in a Monte Carlo type Lagrangian simulation code. Predictions provided by this code, which includes the probabilistic interparticle collision model of Oesterlé and Petitjean (1991, 1993), are compared with the present experimental measurements. Results are discussed and some physical reasons are given to explain the particle behaviour in this specific flow configuration.

## 2. Experimental set-up

The experimental set-up is sketched in Fig. 1. It is composed of a vertical duct, a particle feeder and a photographic visualization device.

### *2.1. Vertical duct and particle feeder*

In order to produce a flow where collisions between particles are significantly influential, a particular geometry has been chosen for the duct, namely a vertical convergent channel with a rectangular cross-section. This channel is made of glass which enables optical measurements of the flow. Its inner dimensions are given in Fig. 2a. The particle feeder, located above the top section of the duct, is made up of a container in which particles are stored before being released into the channel through a rectangular perforated steel plate (Fig. 2b). The particle flow rate can be varied by using plates with different array densities of the regularly spaced cylindrical holes (4 mm in diameter). In order to get a steady and well-defined particle supply conditions, uniform distribution and zero initial velocity of the particles in the inlet section of the duct were ensured by slightly vibrating the perforated plate.

The duct can be subdivided into three parts (Fig. 2a). In the upper region, particles are falling vertically, without any collision between them or with the walls, and under the sole effect of gravity, the surrounding fluid (air) being initially at rest. During their free fall, particles are accelerated up to a velocity of about 3.5 m/s. The second part of the channel is a convergent section made up of two inclined side walls, 30° with the vertical, which lead to numerous particle–wall collisions. Trajectories of colliding particles are then modified and the resulting crossing of the oblique trajectories with those of particles which keep on falling

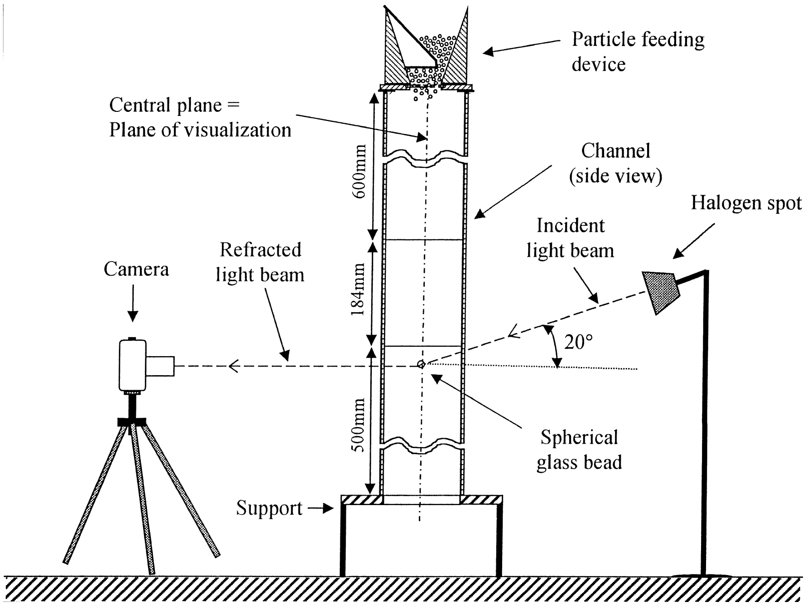

Fig. 1. Experimental arrangement.

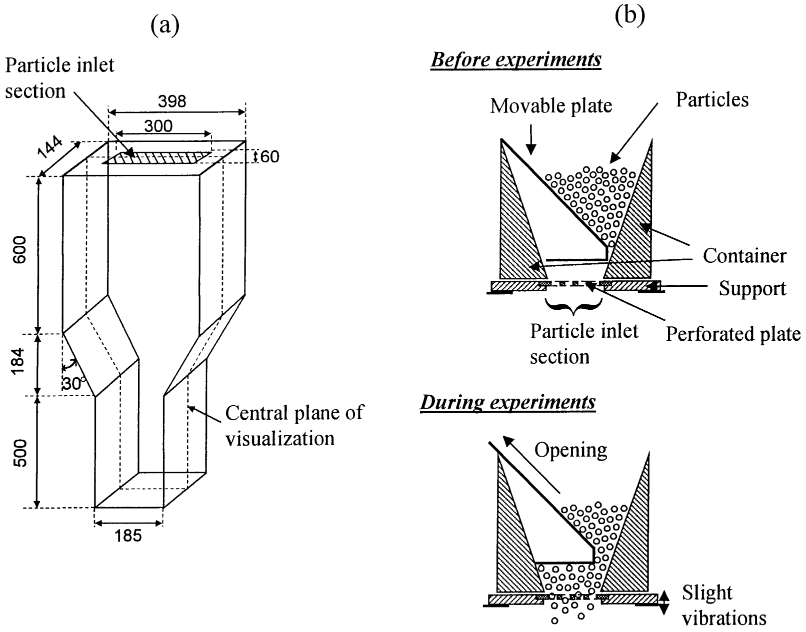

Fig. 2. (a) Dimensions of the channel and localization of the plane of visualization and (b) particle feeding device.

vertically starts the process of collisions between particles. Finally, this process is developing throughout the convergent and downstream where the resulting flow can be visualized. This visualization is performed by means of a photographic technique described hereafter (Section 2.2).

The objectives of this study are not only to experimentally investigate a flow where collisions between particles have a preponderant effect, but also to compare measurements with predictions of a Lagrangian numerical simulation. Therefore, we also tried to suppress or, at the very least, to reduce the effects of other phenomena such as fluid turbulence or wall roughness, whose simulation might lead to some uncertainties and would make it difficult to emphasize the effect of interparticle collisions. That is why we chose large spherical particles (3 mm in diameter in the following experiments) with sufficiently high inertia for the influence of turbulence to be negligible. In addition, the choice of smooth glass plates should allow a deterministic computation of particle–wall collision dynamics during simulations. However, the validity of the latter hypothesis will be further discussed in Section 4.

### 2.2. Photographic visualization technique

Measurements of the concentration and velocity profiles of the solid phase were the main objective of present experiments. An optical method of visualization, combining still photography with an image analysis technique based on particle streak velocimetry (PSV), has been developed (Fohanno, 1997; Fohanno and Oesterlé, 1997). A Pentax 6 × 7 camera, fitted with a 135 mm lens, is set in front of the larger side of the duct and is focused on its central plane (Figs. 1 and 2a). Transparent spherical glass particles are illuminated from behind the channel by a halogen spot whose beam makes an angle of incidence of 20° with respect to the horizontal plane. In that manner, particles refract a part of the light horizontally towards the camera lens, so that the obtained photographs include bright segments which represent fragments of particle trajectories, and whose length depends on the time-exposure (Fig. 3). Fitting this time-exposure (about 1/500 s in our experiments) to the mean velocity and concentration of the particles yields sufficiently long segments to get accurate measurements, but without too many crossings or overlappings of these segments that would result in a complex image processing and analysis. In addition, taking photographs with the light from behind yields a dark background having a good contrast with bright segments.

Furthermore, the thickness of the visualized area has to be adjusted in order to take into account a possible particle displacement in the $y$-direction, i.e. the normal direction to the plane of visualization, caused by the collisions between particles. In order to prevent particles which are not in the central area from being recorded, the camera is set to have a depth of field of about 20 mm and this setting is retained during the whole measurements. Therefore, a particle is considered outside the area of visualization when its trajectory appears as out of focus. In that case, the segment representing this trajectory is wider and its brightness is reduced.

### 2.3. Processing and analysis of the photographs

Black and white 400 ISO films (ILFORD HP5 120) have been used for the experiments. They were developed at an equivalent sensitivity of 800 ISO by increasing the duration of development. Prints taken from the negatives were scanned and digitized with a spatial resolution of 0.1 mm per pixel (i.e. velocity resolution 5 cm/s per pixel with a time-exposure of

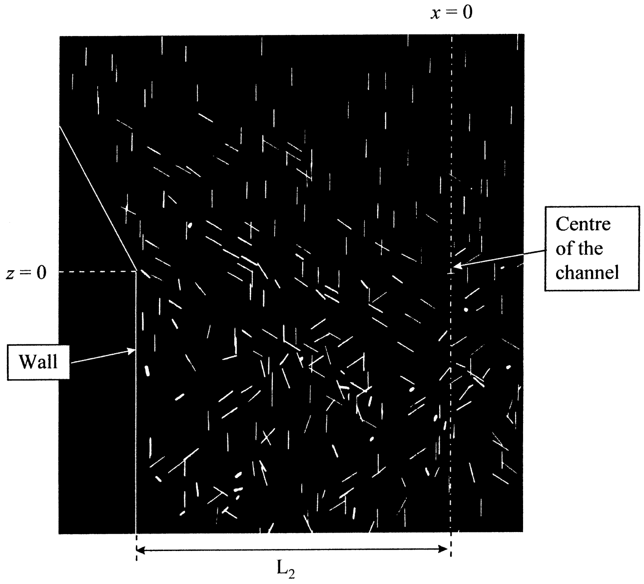

Fig. 3. Example of image (photograph) after processing and before analysis (see Fig. 5 to localize the studied area).

1/500 s) and 256 grey-levels for light intensity. Finally, images are stored on a computer before their processing and analysis. As concerns the time-exposure, 1/500 s is the value indicated on the camera. Actually, the effective time-exposure depends on the mechanical device of the shutter. So, measurements of the time-exposure have been carried out by using a He–Ne laser source and a photoelectric cell placed face to face and on each side of the shutter of the camera. The shutter was activated 200 times consecutively and a device connected with the photoelectric cell was counting the duration of each opening of the shutter. Finally, a mean time-exposure of 1.86 ms was obtained. Furthermore, the present camera is using a focal plane shutter. As a consequence, particles having a displacement in the same direction as the displacement of the shutter are photographed for a longer time than those that are displacing in the opposite direction. This results in an optical deformation, called anamorphosis, giving either a lengthening or a shortening of segments according to particle trajectory directions. Usually, the shutter displacement is far more rapid than the photographed object so that the deformation is negligible. However, in our conditions, we measured an equivalent shutter displacement velocity of 12.9 m/s in the plane of visualization where particle velocities are of the order of 3.5 m/s. This would mean deformation up to about 25% for segment lengths. Therefore, the shutter displacement velocity and direction had to be taken into account in order to correct segment lengths during image analysis.

Image processing consists in removing particle trajectories that do not belong to the area of visualization, according to the above-mentioned criteria. Each image is then binarized before analysis. Owing to the good quality of the contrast, this binarization is performed through a simple determination of the threshold value separating bright segments from the dark background. The objective of the subsequent image analysis is to determine the exact positions of the ends of each segment. From these data, and knowing the time-exposure of the photographs, the position of each particle (middle of the segment) as well as the axial ($V_z$) and transverse ($V_x$) components of the velocity can be obtained. This analysis can be subdivided into two parts. First, the main direction of each segment and the approximate localization of its ends (Fig. 4a) is performed on a binarized and reduced version of the original image (sizes are divided by 3 in order to reduce the computation time). The purpose of the second part of

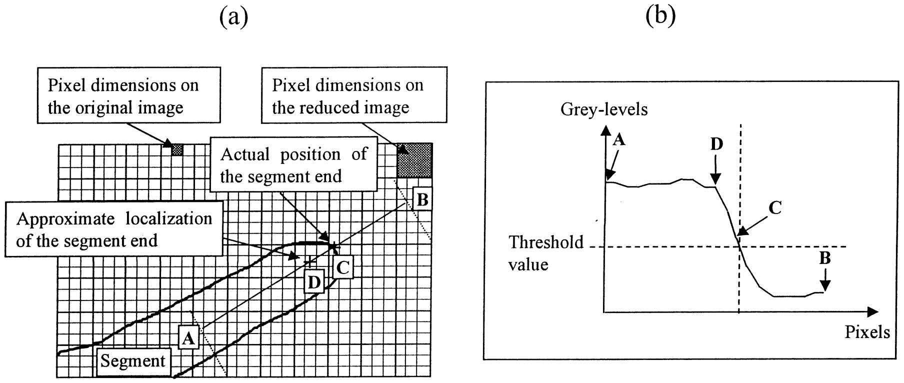

Fig. 4. Principle of image analysis: (a) approximate localization of segment ends and (b) precise determination of the positions of segment ends.

the analysis is to determine the exact positions of the segment ends on the original non-reduced image. For each segment, the positions of sharp changes of the grey-level are searched on the line corresponding to the main direction of the segment (Fig. 4b).

Finally, the central plane of visualization is subdivided into cells as shown by Fig. 5. In our experiments, the studied area consists of nine horizontal rows, each of them containing eight cells regularly spaced from the left side to the centre of the channel. Each cell contains therefore a number of trajectories ($N$) which are statistically treated, leading to the mean velocity components and their standard deviations in each cell. From these data and the number of particles per cell, we then respectively get the velocity and concentration profiles.

## 3. Profiles of particulate flow properties

### 3.1. Experimental conditions

Dimensions of the channel and of the particle inlet section are indicated in Fig. 2a and the studied area is given in Fig. 2a and 5. This area corresponds to the central plane of the channel on which the camera was focused. By reason of symmetry, only the left side of the channel was investigated. The solid particles were spherical glass beads ($d_p = 3$ mm,$\rho_p = 2500$ kg/m$^3$), and experiments were carried out at two mass flow rates ($\dot{m}_p = 0.13$ and 0.38 kg/s). Results will be given at the three axial positions $z = -66$, $+9$ and $+85$ mm, hereafter denoted by zones A, B, C respectively (Fig. 5). Statistics have been performed by analysing 28 photographs for $\dot{m}_p = 0.13$ kg/s and 20 photographs for $\dot{m}_p = 0.38$ kg/s, which means that the number of trajectories per cell ($N$) was between 25 and 130, depending on the particulate mass flow rate and the local concentration. This somewhat low sampling rate may result in some uncertainties which can be

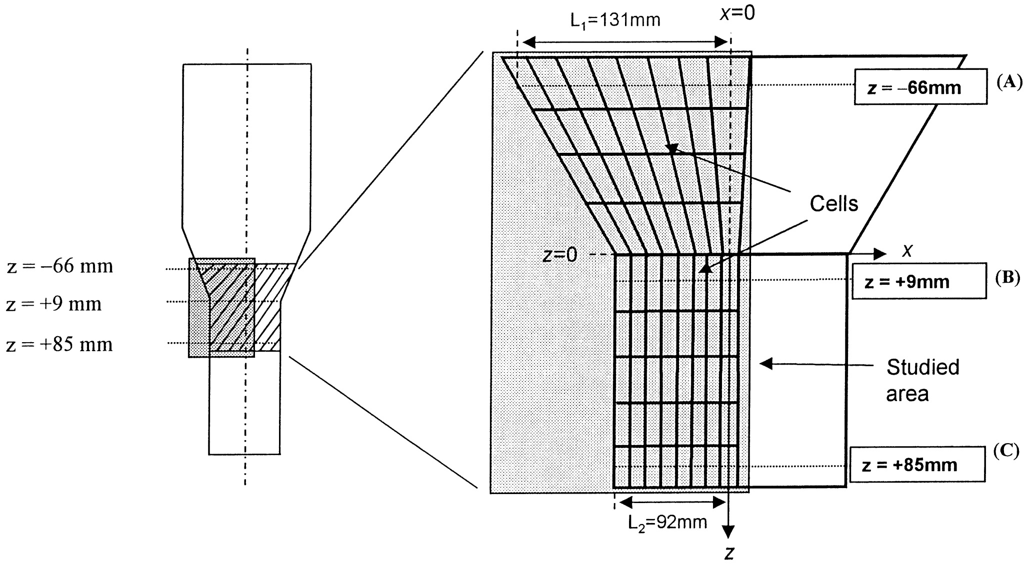

Fig. 5. Front view of the plane of visualization with the studied area.

assessed from the 95% confidence interval. So, the error on the mean particle velocity is about ±13% for $\dot{m}_\mathrm{p} = 0.13$ kg/s and ±10% for $\dot{m}_\mathrm{p} = 0.38$ kg/s. For the standard deviation of the transverse velocity, the uncertainty can be estimated at ±20% and ±15%, respectively.

The particle mean volume fractions downstream the convergent were respectively $\langle \alpha \rangle \approx 6.5 \times 10^{-4}$ and $\langle \alpha \rangle \approx 1.9 \times 10^{-3}$. We are therefore in the case of moderately concentrated flows where the effects of particle-to-particle collisions on the evolution of the flow are no longer negligible (Tanaka and Tsuji, 1991). Moreover, such a collision process is accentuated owing to the above-described particular geometry of the channel (Section 2.1).

### *3.2. Description of the flow*

When the collision process has begun in the converging area, two main kinds of particles can be identified according to their trajectories. On the one hand, we find particles with vertical downward trajectories, which are still freely falling without any interactions with the walls or with other particles. On the other hand, we find particles coming from the inclined plates, after rebounding on them, which exhibit oblique trajectories that make them moving from one side of the channel to the other. These transverse displacements locally increase the solid phase concentration, by adding particles to those which are vertically falling, as shown by Fig. 6 which depicts the velocity and concentration profiles in the three test sections. The concentration increase, which is seen to match the axial velocity decrease, is following the displacement of the transverse particle flow. Higher concentration and lower velocity are first observed near the wall (zone A) before propagating towards the centre of the channel (zone B) and then joining the other side of the channel (zone C, keeping in mind the symmetry of the flow). Another effect of the crossing of the particle flow is to yield relative transverse velocities (up to about 2 m/s) between the two kinds of particles (with vertical or oblique trajectories). In the upper test section (zone A), the transverse motion is characterized, for both particle mass flow rates, by a standard deviation $\sigma(V_x)$ which is about 1.5 m/s near the wall, due to particle–

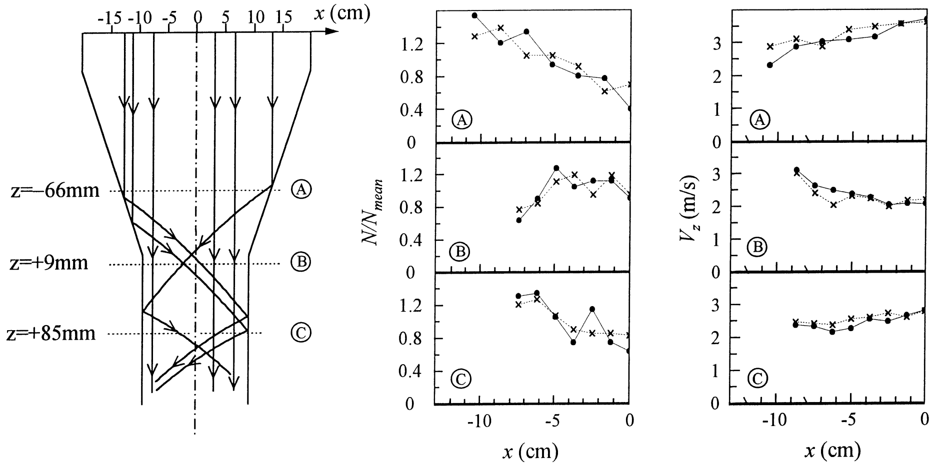

Fig. 6. Dimensionless concentration and particle axial velocity ($V_z$) profiles as functions of particulate mass flow rate (—•— $\dot{m}_\mathrm{p} = 0.13$ kg/s, — × — $\dot{m}_\mathrm{p} = 0.38$ kg/s) and axial position (zones A, B, C from top to bottom).

wall collisions, but remains close to zero at the centre of the channel where we still only have vertically falling particles (Fig. 7a). Lower in the channel, at $z = +9$ mm (zone B), i.e., just below the convergent, the oblique flows coming from each inclined side wall begin to cross one another at the centre of the channel. In that case, we get relative transverse velocities up to 4 m/s which explain the growth of the standard deviation $\sigma(V_x)$ up to 2.5 m/s. This effect persists lower in the channel, with a slight homogenization of the particle agitational motion. It can be noticed that, contrary to the vertical velocity and concentration profiles, the intensity of the transverse motion is notably modified with increasing particulate mass flow rate. Such effects, which can also be observed for the velocity magnitude in the vertical plane $(x,z)$, $V = \sqrt{V_x^2 + V_z^2}$, whose profiles are displayed in Fig. 7b, will be discussed in the next section (Section 3.3).

For freely falling particles, without any interactions with the walls or with other particles, $V$ is equal to the axial velocity, as it is still the case in the centre of the channel at $z = -66$ mm (zone A). Nevertheless, when particles rebound on the inclined plates, some of their momentum, initially located in the plane of visualization, is lost. This can be observed from Fig. 7b, where the velocity magnitude in the vertical plane is seen to decrease for both mass flow rates when progressing downwards the channel. Although this can partly be explained by the momentum transfer from $(x,z)$ plane towards the spanwise direction $y$, which will be discussed further on (Section 3.3), the main cause of such a decrease in the velocity magnitude lies in the fact that actual collisions (particle–wall or particle–particle) are inelastic and that friction is present during the contact. Besides the corresponding energy dissipation, it must be kept in mind that friction leads to a transformation of some of the translational kinetic energy of the particles, whose angular velocity is initially zero, into rotational kinetic energy.

In our experimental conditions, where we are in presence of rather low normal impact velocities (about 2 m/s), the normal coefficient of restitution of particle–wall impacts has been

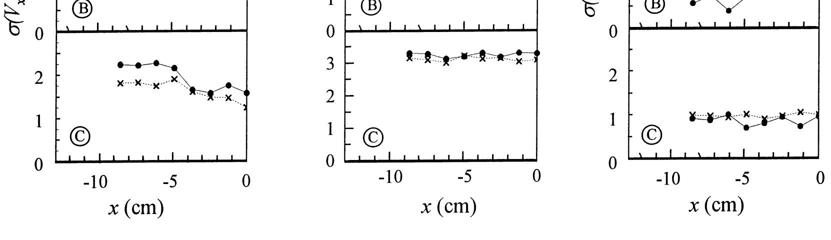

Fig. 7. Particle velocity profiles as functions of particulate mass flow (—●— $\dot{m}_p = 0.13$ kg/s, — × — $\dot{m}_p = 0.38$ kg/s) and axial position (zones A, B, C from top to bottom). (a) Transverse velocity standard deviation $\sigma(V_x)$, (b) velocity magnitude $V$ in the plane of visualization, (c) transverse velocity standard deviation $\sigma(V_z)$.

experimentally investigated (see Section 4), and a value of 0.96 was measured, indicating nearly elastic particle–wall collisions. It can therefore be inferred that the observed decrease of the velocity magnitude is mainly due to the friction induced rotating motion.

### 3.3. Effect of the particulate mass flow rate

Looking at the plots in Fig. 7a shows that the standard deviation of the transverse velocity is reduced at higher particulate mass flow rate, this observation remaining valid throughout the flow. Such a difference between the standard deviations originates from the particle-to-particle collision process, which starts when some particles rebound on the inclined plates and get oblique trajectories crossing the vertical ones, resulting in high deviations of the transverse velocity $V_x$. Despite the crossing of the trajectories, assuming that no particle-to-particle collisions occur would lead to identical profiles, because the percentage of particles rebounding on the inclined plates is always the same whatever the particulate mass flow rate. Nevertheless, collisions between particles effectively occur with a probability which is proportional to the concentration (or particle volume fraction) of the particulate phase. The main effect of such collisions consists in reducing high magnitudes of the transverse velocities that particles get when they rebound on the inclined plates. Therefore, transverse velocities fluctuations are attenuated. Moreover, this attenuation is all the more rapid as the particle concentration is high, which gives an explanation of the observed difference between standard deviations.

Such an attenuation of the magnitude is also observed when looking at the evolution of the velocity magnitude in the vertical plane $V$ as a function of the particulate mass flow rate (Fig. 7b). At first, we note that the magnitude of the velocity is decreasing, in both cases ($\dot{m}_\mathrm{p} = 0.13$ and 0.38 kg/s), when following the flow. Some explanations have previously been given to this decrease such as the inelasticity of particle–wall impacts and the gain of rotational kinetic energy due to the frictional nature of the contacts. However, we also have to take into account the effect of collisions between particles, which is only negligible at the very beginning of the studied area ($z = -66$ mm). As a matter of fact, even if we initially had a strictly two-dimensional flow configuration, collisions between particles always would remain a three-dimensional phenomenon. Consequently, we also have to take into account the direction $y$ normal to the plane of visualization. When two particles collide, some of their initial momentum is transferred towards the normal direction, unless the particles move exactly in the same vertical plane. This momentum transfer is partly explaining the decrease of the velocity magnitude $V$. Moreover, the velocity decrease is more important at high particle flow rate (Fig. 7b, zone B), as could be expected since collision frequency is increasing with increasing concentration. It can also be seen from Fig. 7b that the velocity still decreases between $z = +9$ mm (zone B) and $z = +85$ mm (zone C) for the lower flow rate, contrary to the higher where the decrease is already stopped at $z = +9$ mm. In the first case, the process of collisions between particles keeps on expanding, whereas it is already fully developed in the second case.

### 3.4. Particle fluctuating motion

Experimental measurements performed in the converging gas–solid flow have shown some significant effects of the collisions between particles. At first, increasing the mass flow rate has been observed to reduce the standard deviation of the transverse velocity, i.e. of the fluctuations of the transverse velocity initially caused by particle–wall collisions. In the same time, the axial velocity standard deviation $\sigma(V_z)$, of order of 1 m/s, is found to be almost constant when the collision process has begun (Fig. 7c). Moreover, at $z = +85$ mm (zone C), we can even note a slight increase of $\sigma(V_z)$ with increasing mass flow rate (zone C). Therefore, the initial anisotropy of particle velocity fluctuations is reduced and a process of isotropisation of fluctuating motion, caused by collisions between particles, appears as observed by He and Simonin (1994) and Tanaka and Tsuji (1991) in their numerical studies of vertical gas–solid flows.

This effect is also noticed when looking at the evolution of the distribution of axial and transverse particle velocity fluctuations. Let $V_i$ be the instantaneous particle velocity component in the direction $i$, we have:

$$V_i = \bar{V}_i + v_i \tag{1}$$

where $\bar{V}_i$ is the mean particle velocity component and $v_i$ is the particle velocity fluctuating component. Fig. 8 represents the axial velocity fluctuation ($v_z$) as a function of the transverse velocity fluctuation ($v_x$) at the same three axial locations ($z = -66$, $+9$ and $+85$ mm). For a given axial location, all particles have been taken into account, from the side wall to the centre of the channel.

At $z = -66$ mm (zone A), we still only have two kinds of particle trajectories, as previously indicated in Section 3.2, i.e. vertical ones and oblique ones coming from the left side of the channel. Particles with vertical trajectories do not have any transverse velocity component (i.e. $V_x = 0$), whereas the transverse velocities of rebounding particles are such that $V_x > \bar{V}_x > 0$. As a consequence, $v_x < 0$ for vertically falling particles and $v_x > 0$ for rebounding particles. These two groups of particles are clearly observed on Fig. 8 where they are respectively located in the second ($v_x < 0, v_z > 0$) and fourth ($v_x > 0, v_z < 0$) quadrants. We can also note that all these particles are located along a characteristic oblique direction. However, some particles do not belong to any of these two groups and the location of their velocity fluctuations is quite dispersed. Such particles have already undergone a collision with another particle. At $z = +9$ mm (zone B), two situations have to be considered according to the transverse location ($x$-coordinate) of particles. First, let consider particles located near the wall. In that case, we have the same kinds of particle trajectories as those previously observed at $z = -66$ mm. The distribution of particle velocity fluctuations is similar to the previous case with two small groups of particles located along the same oblique direction. However, this concerns a relatively limited number of particles because of the low particle concentration near the wall. Now, as concerns particles near the centre of the channel, their concentration is higher because of the additional presence of rebounding particles coming from the other side of the channel. By reason of symmetry, due to the presence of opposite oblique flows of particles, the mean transverse velocity is almost zero near the centre of the channel, i.e. $\bar{V}_x \approx 0$. As a consequence $v_x \approx 0$ and $v_z > 0$ for vertically falling particles. As concerns rebounding particles $v_x \approx V_x$ and $v_z < 0$. Therefore, we get three groups of particles clearly positioned on Fig. 8. Nevertheless, the effect of collisions between particles is more accentuated and we can also observe a greater number of particles whose velocity fluctuations are distinctly separated from the above-

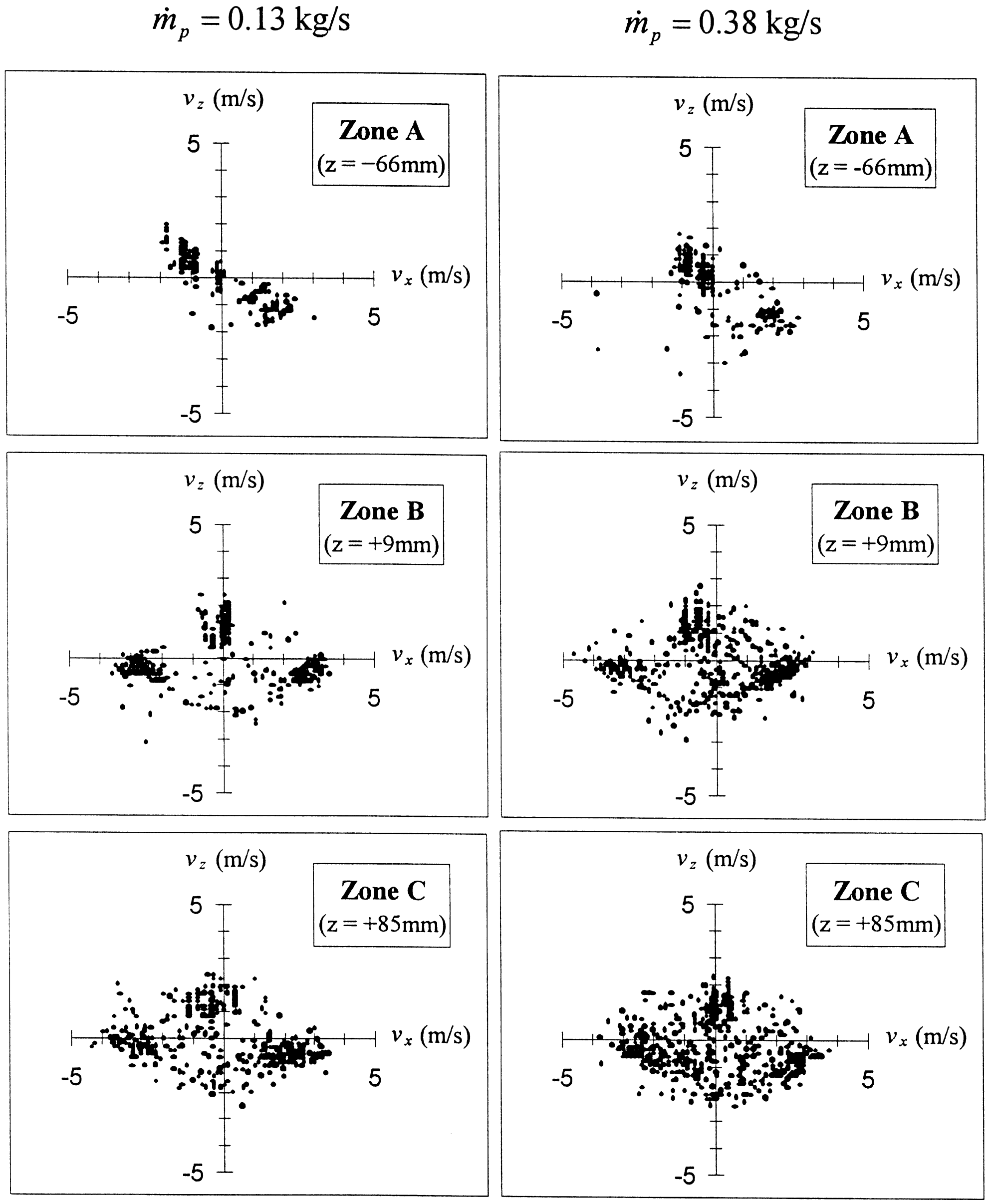

Fig. 8. Distribution of axial and transverse particle fluctuating velocities ($v_z$ and $v_x$) as functions of particulate mass flow rate $\dot{m}_\mathrm{p}$ and axial position (zones A, B, C from top to bottom).

mentioned groups. This effect is more marked at the higher particle mass flow rate. At $z = +85$ mm (zone C), such groups of particles along the oblique direction are no longer observed because rebounding particles coming from the right side wall of the channel have already reached the left side. As a consequence, the simultaneous presence of the three kinds of particle trajectories is now predominant. However, this predominance is decreasing in favor of particles that do not belong to any of these groups. Particle fluctuating velocities are more and more homogeneously distributed, mainly because of particle-to-particle collisions. This trend towards homogeneity is still more marked with the highest particle mass flow rate.

So, we can conclude that particle-to-particle interactions make the flow more homogeneous by attenuating the transverse displacements and uniformly distributing particle velocity fluctuations, and the result is a flow tending towards a merely vertical flow with a decreasing particle fluctuating motion. At $z = +85$ mm (zone C), the same trend can also be observed for the concentration profiles, which are a bit more flattened for the higher mass flow rate (Fig. 6). However, this flattening should be confirmed by further measurements in order to get more accurate results.

Another effect of the collisions is the momentum transfer in the direction normal to the initial plane of the flow (Section 3.3). This has been observed through the attenuation of the velocity magnitude $V$ and of the transverse velocity standard deviations $\sigma(V_x)$, which can only be explained by collisions between particles, whose frequency of occurrence is approximately proportional to the concentration of the particulate phase. In spite of the initial two-dimensional configuration of the flow, we unequivocally have a three-dimensional flow configuration because of collisions between particles. Moreover, particle-to-particle collisions may not be the only cause of this three-dimensional configuration of the flow. It may also be caused by the roughness of the walls or the departure from sphericity, even small, of the particles. In that case, the plane in which particle–wall collisions occur is no longer restricted to the original plane of motion. As a matter of fact, this three-dimensional aspect should always be kept in mind when experimentally or numerically studying such collisional flows. As a consequence, the present results show some interesting features of the studied flow which will be useful for future comparisons with predictions by three-dimensional Lagrangian numerical simulations or by Eulerian computations (two-fluid models).

## 4. Investigation of particle–wall collision parameters

Particle–wall collisions play such a significant role on the evolution of confined gas–solid flows (Matsumoto and Saito, 1970a, 1970b; Tsuji et al., 1985; Sommerfeld, 1992) that it is absolutely necessary to take them into account in numerical simulations. In that case, the classical representation of particle–wall collision dynamics consists in considering inelastic, frictional contacts by means of the coefficient of restitution of the normal velocity component ($e_{nw}$) and by application of Coulomb's law on friction. In the following, subscripts $w$ and $p$ will respectively indicate particle–wall and particle-to-particle collision parameters. Lun and Savage (1987) proposed an improvement of this model, by introducing a tangential restitution coefficient, that was recently applied for the numerical simulations of gas–solid flows (Lun and Bent, 1994; Lun and Liu, 1997). However, whatever the model used, it always requires the knowledge of parameters (coefficients) which essentially depend on the actual nature of the contact and, consequently, of the experimental conditions. Each flow having its own characteristics (properties of particle and wall materials, roughness of the wall surface,...), an experimental investigation of particle–wall collision properties of the vertical gas–solid flow under study has been conducted. As concerns the particle-to-particle collisions, the same impact model has been introduced in the simulation code. However, it is quite more difficult to perform experimental measurements on such collisions and some assumptions, detailed hereafter, have been made to choose the values of the coefficients used in the model.

At first, the main characteristics of the impact model are briefly recalled. Then, the experimental apparatus and procedure used to determine the particle–wall collision parameters are described. Finally, results of measurements are presented and commented.

### 4.1. Impact model

The impact model will not only be used to model the particle–wall collision dynamics but also the particle-to-particle one. Therefore, for generality, the case of two spheres will be considered, a plane wall being the particular case of a sphere of infinite radius and mass. A sketch of the impact of two perfectly spherical particles of masses $m_1$ and $m_2$, radii $R_1$ and $R_2$, and centres $O_1$ and $O_2$, is given in Fig. 9. The collision plane is defined by the unit vectors **n** and **t**, where **n** is the normal direction joining the particle centres and **t** is a vector which also belongs to the tangential plane of the two spheres at the point of contact $M$. $\mathbf{k} = \mathbf{n} \times \mathbf{t}$ is the third unit vector, normal to the collision plane. Linear and angular velocities will be respectively denoted by $\mathbf{V}_1$ and $\Omega_1$ for the first particle, and $\mathbf{V}_2$ and $\Omega_2$ for the second.

Let $\mathbf{V}_1^*$ and $\mathbf{V}_2^*$ be the peripheral velocities of the spheres, we have:

$$\mathbf{V}_1^* = \mathbf{V}_1 - R_1(\mathbf{n} \times \Omega_1)$$

$$\mathbf{V}_2^* = \mathbf{V}_2 - R_2(\mathbf{n} \times \Omega_2) \tag{2}$$

Therefore, the relative velocity $\mathbf{V}_R$ between the two spheres at the point of contact is:

$$\mathbf{V}_R = \mathbf{V}_1^* - \mathbf{V}_2^* = \begin{cases} V_{Rn} = V_{1n} - V_{2n} \\ V_{Rt} = V_{1t} + R_1\Omega_{1k} - V_{2t} + R_2\Omega_{2k} \\ V_{Rk} = V_{1k} - R_1\Omega_{1t} - V_{2k} - R_2\Omega_{2t} \end{cases} \tag{3}$$

In this model, inelasticity is taken into account by using Newton's hypothesis which assumes a constant ratio between the post- and pre-collisional normal velocity components. This ratio

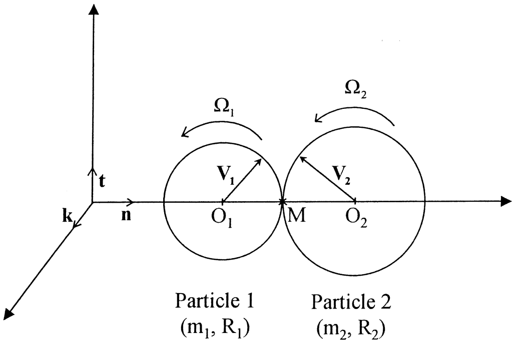

Fig. 9. Sketch of the impact of two spherical particles.

defines the coefficient of restitution of the normal velocity component $e_n$:

$$e_n = -\frac{V'_{1n} - V'_{2n}}{V_{1n} - V_{2n}} \tag{4}$$

where primes denote post-collisional velocities.

Now, the application of Coulomb's law on friction allows the distinction between sliding and non-sliding contacts. Let $\mathbf{V}_s$ be the *sliding velocity*, $\mathbf{V}_s = V_{Rt}\mathbf{t} + V_{Rk}\mathbf{k}$, corresponding to the tangential relative velocity between the two spheres at the point of contact $M$. If the frictional force is not sufficient to stop sliding during the collision time, a relative tangential velocity will still exist after the impact (i.e. $|\mathbf{V}'_s| > 0$). According to Coulomb's law, this kind of sliding contact occurs when the following relationship is satisfied:

$$|\mathbf{J} \times \mathbf{n}| > \mu_s |\mathbf{J} \cdot \mathbf{n}| \tag{5}$$

where $\mu_s$ is the coefficient of static friction and $\mathbf{J}$ is the impulse of particle 1 on particle 2:

$$\mathbf{J} = m_1(\mathbf{V}_1 - \mathbf{V}'_1) = -m_2(\mathbf{V}_2 - \mathbf{V}'_2) \tag{6}$$

In that case, the tangential impulse components ($J_t$ and $J_k$) are given by:

$$J_t = -\mu_k J_n \frac{V_{Rt}}{\sqrt{V^2_{Rt} + V^2_{Rk}}}$$

$$J_k = -\mu_k J_n \frac{V_{Rk}}{\sqrt{V^2_{Rt} + V^2_{Rk}}} \tag{7}$$

where $\mu_k$ is the coefficient of kinetic friction and $J_n$ is the normal impulse component which can be written, from relationships (4) and (6):

$$J_n = -\frac{m_1 m_2}{m_1 + m_2}(1 + e_n)(V_{1n} - V_{2n}) \tag{8}$$

Eq. (6) relates the linear velocities before and after collisions. Similarly the angular momentum conservation leads to:

$$I_1(\Omega'_1 - \Omega_1) = \mathbf{O}_1\mathbf{M} \times \mathbf{J}$$

$$I_2(\Omega'_2 - \Omega_2) = \mathbf{O}_2\mathbf{M} \times \mathbf{J} \tag{9}$$

where $I_i = (2m_i R_i^2)/5$ $(i = 1{,}2)$ are the moments of inertia of the two spherical particles. Therefore, knowing the pre-collisional linear and angular velocities, the post-collisional velocities are easily deduced from relationships (3) and (6)–(9).

On the other hand, if relationship (5) is not satisfied, a non-sliding contact takes place. This means that $|\mathbf{V}'_s| = 0$ at the end of collision time. Eq. (8) can still be used to find the normal component of the impulse, whereas the tangential components are simply deduced from relationships (3), (4) and (6), that is:

$$J_t = -\frac{2}{7} V_{Rt} \frac{m_1 m_2}{m_1 + m_2}$$

$$J_k = -\frac{2}{7} V_{Rk} \frac{m_1 m_2}{m_1 + m_2} \tag{10}$$

Replacing Eq. (7) by (10), post-collisional linear and angular velocities can be deduced in the same manner as indicated for the sliding case.

### 4.2. Apparatus and procedure

Several experimental studies on particle–wall collision properties have been carried out, among which we can mention the recent works of Sommerfeld (1992), Schade et al. (1996) and Schade and Hådrich (1998). As concerns particle-to-particle impacts, few studies exist due to the more complex setting of such experiments. However, interesting experimental results about the collision dynamics of two spheres can be found in the work of Foerster et al. (1994), recently improved by Lorenz et al. (1997).

Measurements described in the present section relate to particle–wall impact properties. Glass particles are released one by one from a particle feeder which ensures nearly zero initial spin. Each particle is then freely falling in quiescent air, and accelerated by gravity, before impacting a 8 mm-thick glass plate corresponding to the material whose the vertical duct is composed of. This plate is fixed on a support which can be variably inclined with angular positions going from 0° to 90° with respect to the vertical. Finally, particle trajectories are visualized near from the impact point by means of a stroboscopic lighting. An example of a typical image obtained in this manner is given by Fig. 10.

### 4.3. Measurements and results

Since the collision parameters may generally depend on the impact velocity and angle, the experimental device was set up to match the conditions encountered in our vertical convergent channel. In the experiments described in Sections 2 and 3, the particle velocities before impact on the side walls are of the order of 3.5 m/s. Such a velocity is reached by a particle falling from a height of about 70 cm, therefore this distance has been imposed between the glass plate and the outlet of the particle feeder. Still referring to the vertical duct experiments, the impact angle is 30° for the first particle–wall collisions; however, it may vary in a broader range for the following collisions. That is the reason why we also investigate the influence of this angle upon the collision parameters, performing four series of measurements with impact angles of 20°, 30°, 45° and 60°.

Analysis of the measurements will be performed using the collision model described in Section 4.1, assuming plane collision, i.e. $V_{1k} = V'_{1k} = 0$ (Fig. 11). Then, applying this model to the case of a particle–wall collision (infinite radius $R_2$ and mass $m_2$), and a priori assuming sliding contacts, the coefficient of restitution $e_{nw}$ and the coefficient of kinetic friction $\mu_{kw}$ are

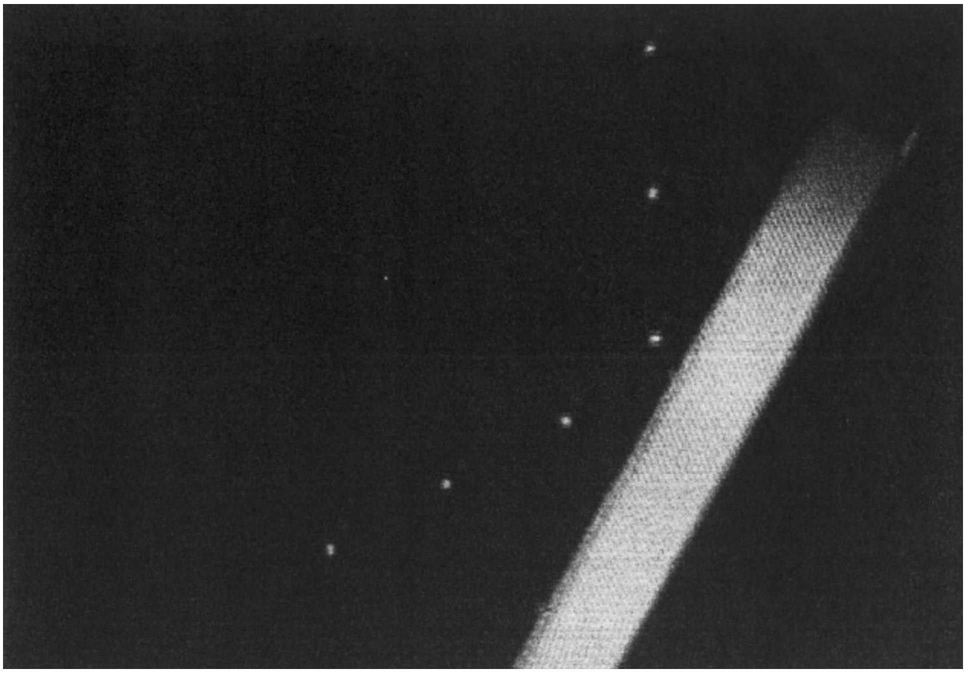

Fig. 10. Stroboscopic image of the trajectory of a 3 mm-diameter spherical glass bead impacting a 8 mm-thick glass plate with an angle of 30°.

respectively given by:

$$e_{nw} = \frac{|V'_{1n}|}{|V_{1n}|} \tag{11a}$$

and

$$\mu_{kw} = \frac{|V'_{1t} - V_{1t}|}{(1 + e_{nw})|V_{1n}|} \tag{11b}$$

In that case, using relationships for a sliding contact, the sliding condition is given by:

$$\mu_{kw} \leq \frac{2}{7}\frac{|V_{1t} + R_1\Omega_{1k}|}{(1 + e_{nw})|V_{1n}|} \tag{12}$$

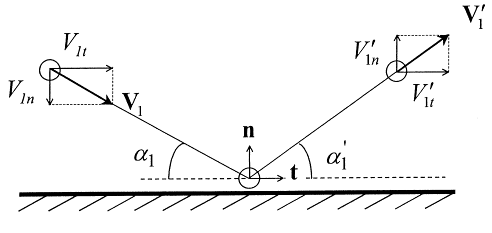

Fig. 11. Sketch of the rebound of a particle on a plane wall.

Moreover, the experimental apparatus has been conceived in such a manner that the spherical particle has no spin before impact ($\Omega_{1k} = 0$). Introducing $\tan \alpha_1 = |V_{1n}|/|V_{1t}|$, the condition (12) becomes:

$$\mu_{kw} \leq \frac{2}{7(1 + e_{nw})\tan \alpha_1} \tag{13}$$

In short, the first step of the experimental data processing consists in calculating the pre- and post-collisional velocity components, as well as the impact and rebound angles (respectively $\alpha_1$, $\alpha_1'$, see Fig. 11). Then, assuming a sliding collision, the coefficients $e_{nw}$ and $\mu_{kw}$ are determined from Eqs. (11a) and (11b). Finally, the validity of the sliding condition hypothesis is checked according to Eq. (13).

The results obtained under the above-mentioned experimental conditions are summarized in Table 1. The coefficient of restitution of the normal velocity keeps quite constant whatever the impact angle. Furthermore, its value, close to 1, indicates nearly elastic collisions. This feature is probably due to the relatively low magnitude of impact velocity, not sufficient to allow notable plastic deformation at the contact area (Walton, 1993). It can be seen from Table 1 that the coefficient of kinetic friction exhibits low and quite constant values, although a slight increase may be noticed with increasing impact angle. This corresponds to relatively smooth contacts as it could be expected because of the nature of the wall and particle materials. However, it must be mentioned that the measurements have been performed with clean and unworn glass plates, even though particles have already been used in the vertical duct experiments. As a consequence, the actual nature of particle–wall contacts, especially as concerns the friction and the roughness of the glass plates, may differ from these experiments. This observation should be kept in mind when comparing the experimental measurements of Section 3 with predictions of the numerical simulation in the next section. Moreover, as concerns the coefficient of static friction $\mu_{sw}$, it can be assessed from the measurements by determining the limit between sliding and non-sliding contacts. Obviously, this limit is reached for an inclination $\alpha_{1L}$ comprised between 45° and 60°. As $\mu_{sw} \geq \mu_{kw}$, and having $\mu_{kw} \approx 0.14$ for an inclination of 45°, we can estimate that the coefficient of static friction is about 0.20. This value will be used in the first numerical simulations of Section 5. However, the choice of this value and its consequences on the accuracy of the numerical predictions will be discussed in Section 5.3.

Table 1
Particle–wall collision properties

| $\bar{\alpha}_1$ (°) | $\bar{V}_1$ (m/s) | $\bar{e}_{nw}$ | $\bar{\mu}_{kw}$ | $2/7(1 + \bar{e}_{nw})\tan \bar{\alpha}_1$ | Verification of sliding condition |
|---|---|---|---|---|---|
| 17.6 | 3.32 | 0.98 | 0.09 | 0.45 | Yes |
| 26.6 | 3.64 | 0.96 | 0.11 | 0.29 | Yes |
| 40.04 | 3.47 | 0.96 | 0.14 | 0.17 | Yes |
| 57.8 | 3.43 | 0.95 | 0.14 | 0.09 | No |

## 5. Comparison with Lagrangian simulation predictions

### 5.1. Simulation principle

Oesterlé and Petitjean (1991, 1993) have previously detailed the principles of the Lagrangian simulation technique and of the probabilistic model used to take into account particle-to-particle collisions. We will briefly recall the main features of this three-dimensional simulation code which makes use of a Monte Carlo type Lagrangian technique allowing the computation of only a limited number of particle trajectories in order to reduce the computational time.

Collisions between particles become influential and have therefore to be taken into account when treating non-dilute flows. In that case, they are introduced by means of a probabilistic model where the expression of the collision frequency is derived from an analogy with the kinetic theory of gases. For the travelling particle of radius $R_1$ and velocity $\mathbf{V}_1$, the collision frequency $\nu$ is written as:

$$\nu = \sqrt{2}\pi(R_1 + R_0)^2|\mathbf{V}_1 - \langle\mathbf{V}_0\rangle|N \tag{14}$$

where $R_0$ and $\langle\mathbf{V}_0\rangle$ are the mean radius and velocity of surrounding particles and $N$ is the concentration (number/m$^3$).

Let $\psi(t_0,t)$ be the probability for a particle to undergo a collision between instants $t_0$ and $t$, so that the probability that no collision occurs is $1 - \psi(t_0,t)$. If we consider a small time interval d$t$, the number of particles which undergo a collision during d$t$ is $\nu\,\mathrm{d}t$. Therefore, the probability of collision between instants $t$ and $t + \mathrm{d}t$ of a particle that does not have undergone any collision between instants $t_0$ and $t$ is:

$$\mathrm{d}\psi = \psi(t_0,t + \mathrm{d}t) - \psi(t_0,t) = \left[1 - \psi(t_0,t)\right]\nu\,\mathrm{d}t \tag{15}$$

Since $\psi(t_0,t_0) = 0$, integration of (15) yields:

$$\psi(t_0,t) = 1 - \exp\left[-\nu(t - t_0)\right] \tag{16}$$

or, with $\Delta t = t - t_0$:

$$\Psi(\Delta t) = \psi(t_0,t_0 + \Delta t) = 1 - \exp(-\nu\Delta t) \tag{17}$$

As a consequence, the probability only depends on the time interval $\Delta t$ corresponding to the time step of the simulation. The probability of collision of the travelling particle with a surrounding particle is calculated at each time step and is compared with a random number, chosen among a uniform distribution between 0 and 1, in order to decide if a collision occurs.

### 5.2. Test of the probabilistic collision model

Simulations have been carried out with and without taking into account particle-to-particle collisions, and for both particulate mass flow rates ($\dot{m}_\mathrm{p} = 0.13$ and 0.38 kg/s) used in experiments. Note that in the case without collisions, we obviously get the same results whatever the particulate mass flow rate. The coefficients of the particle–wall collision model have been experimentally measured (see Section 4), i.e. $e_{nw} = 0.96$ and $\mu_{kw} = 0.12$, and an estimated value of 0.20 has been given to the coefficient of static friction $\mu_{sw}$. Like particle–wall collisions, particle-to-particle collisions are also glass-glass contacts so that the same values have been chosen for the corresponding coefficients of restitution and friction. Furthermore, we can notice that these values are quite similar to particle-to-particle impact properties measured by Foerster et al. (1994) on spherical glass beads 3.18 mm in diameter ($e_{np} = 0.97, \mu_{kp} = 0.092$).

Measurements have been compared with predictions of the Lagrangian simulation, using or not the probabilistic collision model proposed by Oesterlé and Petitjean (1991, 1993). The statistics computed from the numerical predictions were verified not to be significantly affected by any influence of particles having a large velocity in the $y$-direction, which might possibly not appear in the experimental photographs.

Experimental measurements and numerical predictions, given as dimensionless concentration (Fig. 12), axial velocity (Fig. 13) and transverse velocity standard deviation (Fig. 14) profiles at $z = +85$ mm (zone C), where the collision process is well developed, are compared for both mass flow rates. In each case and for each mass flow rate, a better agreement of predictions with measurements is found when using the probabilistic collision model. However, we still observe that the Lagrangian simulation slightly over-estimates the axial velocity and under-estimates the transverse velocity standard deviation. Possible explanations for such discrepancies may be found in uncertainties concerning the particle–wall collision model such as the choice of the coefficient of static friction $\mu_{sw}$ which determines the limit between sliding and non-sliding contacts and is in fact dependent on the actual nature of the contacts during the experiments. The probabilistic collision model itself may also explain such differences. These potential sources of errors are now going to be investigated.

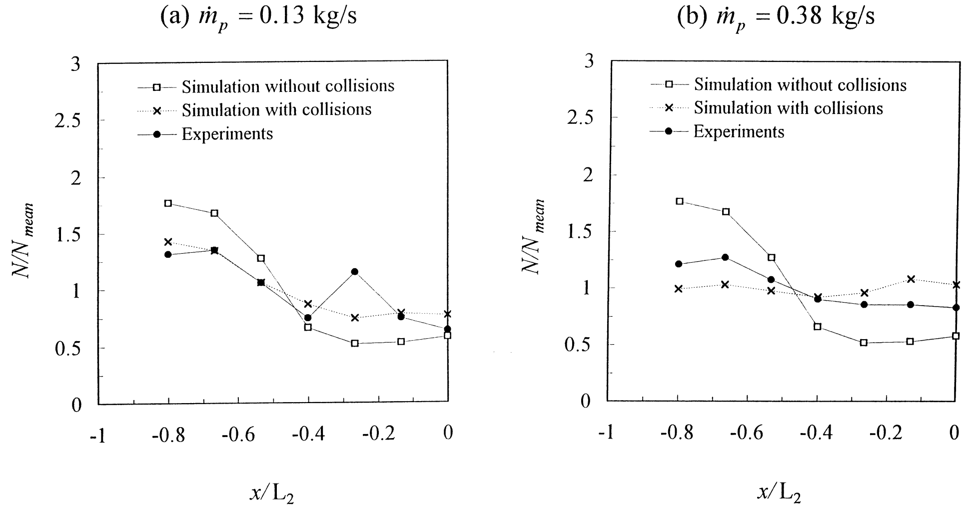

Fig. 12. Comparison of dimensionless concentration measurements, at $z = +85$ mm and for both particulate mass flow rates, with predictions of the Lagrangian simulation using or not the probabilistic collision model. (a) $\dot{m}_p = 0.13$ kg/s and (b) $\dot{m}_p = 0.38$ kg/s.

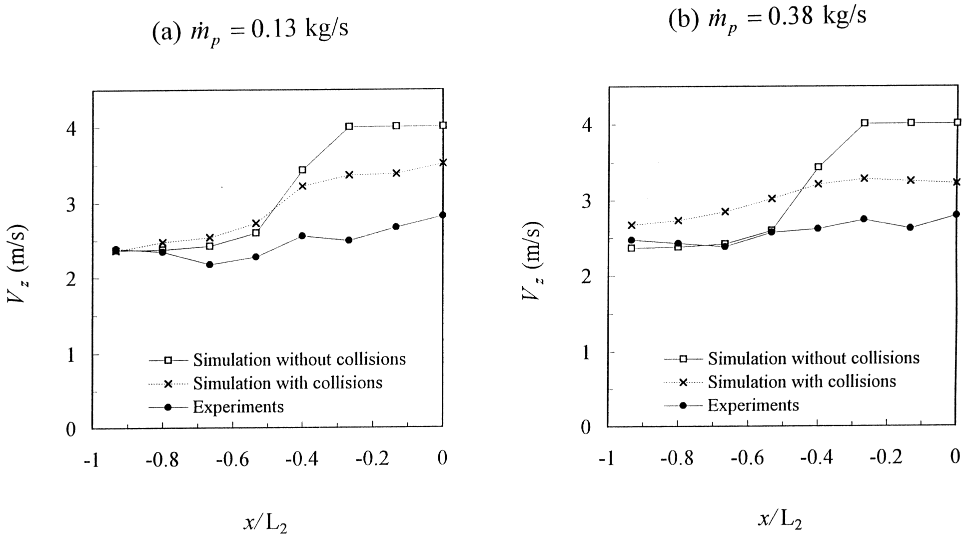
(a) $\dot{m}_p = 0.13$ kg/s

(b) $\dot{m}_p = 0.38$ kg/s

Fig. 13. Comparison of axial velocity measurements, at $z = +85$ mm and for both particulate mass flow rates, with predictions of the Lagrangian simulation using or not the probabilistic collision model. (a) $\dot{m}_p = 0.13$ kg/s and (b) $\dot{m}_p = 0.38$ kg/s.

### 5.3. *Effect of particle–wall contact parameters*

In the previous section (Section 5.2) we used a coefficient of static friction assessed from particle–wall impact properties measured in Section 4. However, in the collisional gas–solid flow under study, the first collision of particles with the lateral inclined walls of the convergent

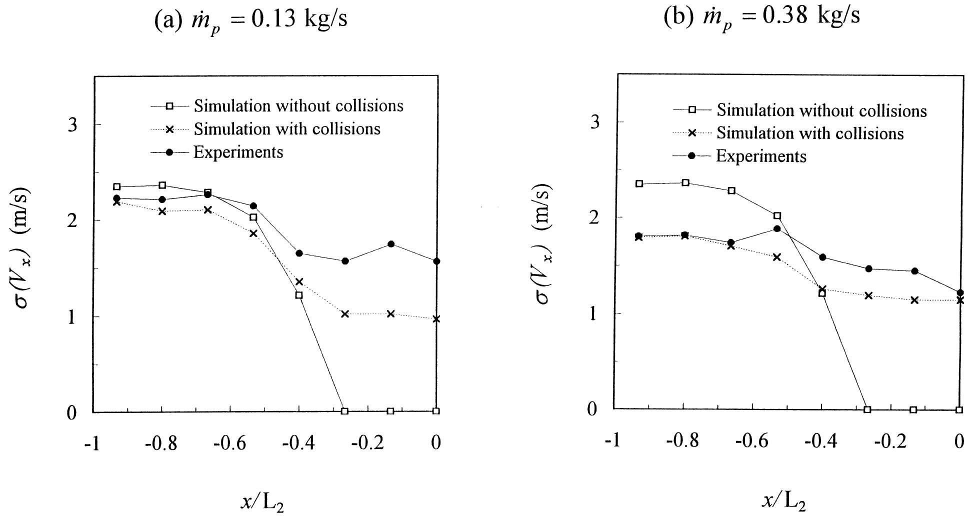
(a) $\dot{m}_p = 0.13$ kg/s

(b) $\dot{m}_p = 0.38$ kg/s

Fig. 14. Comparison of transverse velocity standard deviation measurements, at $z = +85$ mm and for both particulate mass flow rates, with predictions of the Lagrangian simulation using or not the probabilistic collision model. (a) $\dot{m}_p = 0.13$ kg/s and (b) $\dot{m}_p = 0.38$ kg/s.

plays a significant role as already mentioned in Section 3. For this particular collision, impact conditions are nearly always identical, i.e. a pre-collisional particle velocity magnitude of about 3.5 m/s and a vertical downwards particle trajectory making an angle of 30° with respect to the wall. Therefore, normal and tangential particle velocities keep quite constants, i.e. $|V_n| \approx 1.75$ m/s and $|V_t| \approx 3.03$ m/s, and no rotation is assumed before impact. This results in a constant coefficient of restitution given by measurements of Section 4, i.e. $e_{nw} \approx 0.96$, and there is a threshold value for the coefficient of static friction that separates sliding contacts from non-sliding contacts. Let $\mu_{sw}^{T}$ be this coefficient, from relation (5), we get:

$$|\mathbf{J} \times \mathbf{n}| = \mu_{sw}^{T} |\mathbf{J} \cdot \mathbf{n}| \tag{18}$$

As the collision takes place in the plane (**n**,**t**) (Fig. 11), (18) can be rewritten:

$$|J_t| = \mu_{sw}^{T} |J_n| \tag{19}$$

and we finally get:

$$\mu_{sw}^{T} = \frac{2}{7(1 + e_{nw}) \tan \alpha_1} \tag{20}$$

Replacing $\alpha_1$ and $e_{nw}$ by their corresponding values in relation (20), we find $\mu_{sw}^{T} \approx 0.25$. This threshold value is greater than the coefficient estimated in Section 4 and we could conclude that the first collision is always a sliding contact. However, the coefficient of static friction has been determined from ideal experimental conditions where a clean and smooth glass plate has been used as a wall. On the other hand, in the vertical channel we have to take into account some wear of the lateral walls as well as possible dust deposition, due to repeated experiments and to the large number of particle impacts. Therefore, the resulting dirtier and slightly rougher surfaces of the walls may cause more friction and increase the coefficient of static friction in such a manner that the first collision is no longer a sliding contact but a non-sliding one. Now, let us take $\mu_{sw} = 0.40$ in order to be in the non-sliding case. In Fig. 15, the experimental axial velocity profile, at $z = +85$ mm and for the higher particulate mass flow rate ($\dot{m}_{\mathrm{p}} = 0.38$ kg/s), is compared with profiles given by the corresponding numerical simulations where sliding ($\mu_{sw} = 0.20$) and non-sliding ($\mu_{sw} = 0.40$) conditions have been respectively

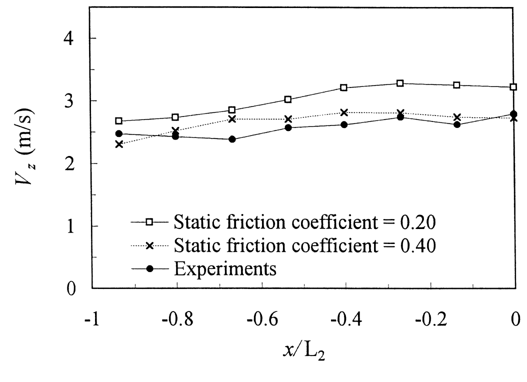

Fig. 15. Effect of friction parameters on axial velocity predictions at $z = +85$ mm and for $\dot{m}_{\mathrm{p}} = 0.38$ kg/s.

chosen. The better agreement obtained with predictions given by the non-sliding case corroborates the assumption that has been made concerning the actual nature of friction during particle–wall contacts.

### 5.4. Choice of the surrounding colliding particle velocity

In the probabilistic collision model, the collision frequency given by relation (14) is used, where $\langle \mathbf{V}_0 \rangle$ is the mean velocity of surrounding particles. In their study, Oesterlé and Petitjean (1991, 1993) assumed a constant velocity for surrounding particles, i.e. $\mathbf{V}_0 = \langle \mathbf{V}_0 \rangle$. However, velocities of surrounding particles are rather fluctuating around the mean velocity. Therefore, the present simulations have been carried out by assuming a Gaussian distribution of $\mathbf{V}_0$ with a mean particle velocity $\langle \mathbf{V}_0 \rangle$ and a standard deviation $\sigma(\mathbf{V}_0)$, this standard deviation being calculated and updated at each time step of the simulation. Furthermore, as particle velocity fluctuations are not isotropic, the standard deviations $\sigma(V_{ox})$,$\sigma(V_{oy})$,$\sigma(V_{oz})$ of each velocity component are separately calculated. The collision frequency, and thus the collision probability, are still determined by using the mean velocity for the surrounding particle velocities. However, when a collision is decided to occur, the velocity components of the effective surrounding colliding particle are now randomly chosen among their Gaussian distributions. Next, the effective velocity of the surrounding particle serves to calculate the post-collisional linear $(\mathbf{V}_1')$ and angular $(\Omega_1')$ velocities of the travelling particle by using the impact model presented in Section 4.1. The effect of such a determination of the velocity is obvious on particle velocity fluctuations as shown by Fig. 16 which compares the measured standard deviation of the transverse velocity $\sigma(V_x)$, at $z = +85$ mm ($\dot{m}_p = 0.38$ kg/s), with the corresponding predictions of simulations with or without consideration of possible velocity fluctuations.

### 5.5. Influence of rotation

Simulations have been carried out with a fluid initially at rest and with the influence of

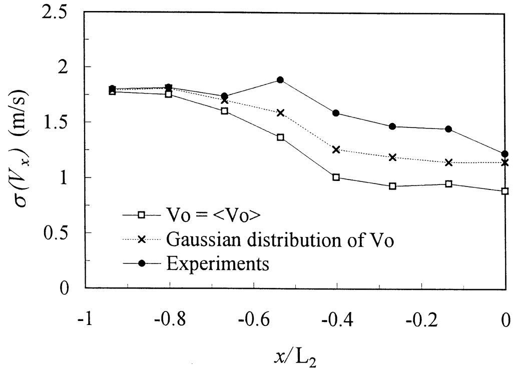

Fig. 16. Effect of the choice of the velocity of the surrounding colliding particle on transverse velocity standard deviation predictions at $z = +85$ mm and for $\dot{m}_p = 0.38$ kg/s.

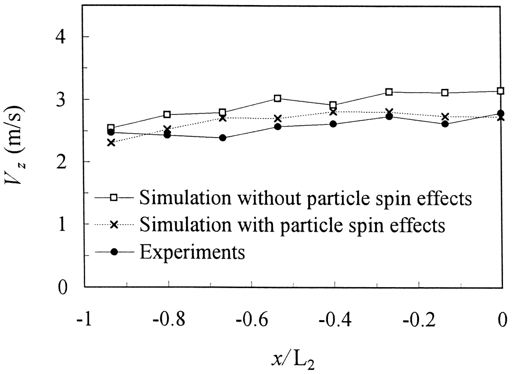

Fig. 17. Particle spin-induced effects on axial velocity predictions at $z = +85$ mm and for $\dot{m}_p = 0.38$ kg/s.

particles on this fluid assumed to be negligible. However, even if we are applying a one-way coupling method, we still have to take into account the effects of the fluid on the particles such as the drag force and the influence of particle rotation. In most numerical simulations, only the drag force is generally considered and is modelled by means of correlations such as the one proposed by Morsi and Alexander (1972), which has been used in our simulations. However, we are concerned here with a confined gas–solid flow where particle–wall and particle-to-particle collisions both play a significant rôle, therefore we can no longer neglect the collision-induced rotation of particles. In this case, the lift force acting on a rotating spherical particle has been expressed by means of a correlation giving the lift coefficient as a function of $Re_p$, as proposed by Oesterlé and Bui Dinh (1998), where $Re_p = (|\mathbf{V}_r| \cdot d_p)/\upsilon_f$ is the Reynolds number based on the particle diameter $d_p$, the kinematic viscosity of the fluid $\nu_f$ and the relative velocity $\mathbf{V}_r = \mathbf{V}_f - \mathbf{V}_p$ between the fluid and the particle. As concerns the hydrodynamic torque, the correlation of Dennis et al. (1980) has been employed. As the fluid is at rest, we can neglect any effect due to shear (no Saffman force).

Finally, looking at the plots on Fig. 17 shows the necessity of considering rotation in such collisional flows. Even in the case of large and heavy particles with rather high inertia, the effect of particle rotation, caused by the frictional nature of the numerous particle-to-particle and particle–wall collisions, is not negligible, and better numerical predictions of the axial velocity, at $z = +85$ mm and with $\dot{m}_p = 0.38$ kg/s, are obtained when such effects are modelled.

## 6. Conclusion

An original experimental facility, allowing the investigation of a particular gas–solid collisional flow of large spherical particles in a vertical duct, was presented. The effect of the solid phase concentration on the evolution of particle velocity characteristics has been observed, as also a reduction of the initial anisotropy of the fluctuating motion of particles caused by collisions between particles. The results demonstrate the suitability of the experimental facility to get measurements needed for testing numerical simulations of flows where collisions between particles are influential.

The comparison of measurements with predictions of a three-dimensional Monte Carlo type Lagrangian simulation code has shown the relevancy of using a probabilistic collision model to take particle-to-particle collisions into account. The slight differences that still exist between measurements and predictions can be partly explained by the significant influence of particle–wall interactions on the flow characteristics. This emphasises the necessity for an accurate knowledge of the parameters used to model particle–wall impacts, which can only be obtained by experimental means. Non-negligible effects of the spin-induced force on such large particles have also been noted.

Any improvement of the predictions will also surely require a better knowledge of the parameters governing the particle-to-particle collision process such as the collision frequency. This could be achieved by directly measuring the distribution of the collision frequency on the vertical channel facility. The development of such a measurement technique is planned and will be useful to test various collision models found in the literature.

## References

Crowe, C.T., 1981. On the relative importance of particle–particle collisions in gas-particle flows. In: Proc. Conf. on Gas-Borne Particles, Oxford, England, Paper C78/81, 135–137.

Dennis, S.C.R., Singh, S.N., Ingham, D.B., 1980. The steady flow due to a rotating sphere at low and moderate Reynolds numbers. J. Fluid Mech 101 (2), 257–279.

Foerster, S.F., Louge, M.Y., Chang, H., Allia, K., 1994. Measurements of the collision properties of small spheres. Phys. Fluids 6 (3), 1108–1115.

Fohanno, S. 1997. Contribution à l'étude des collisions entre particules et des interactions particules-parois en écoulement gaz–solide, par voie expérimentale et simulation lagrangienne. Thèse de Doctorat de l'Université Henri Poincaré, Nancy, France.

Fohanno, S., Oesterlé, B., 1997. Experimental study of interparticle collisions in gas–solid flows. In: Proc. 1997 ASME-FED Summer Meeting, Vancouver, Canada, Paper 97-3613 (CD ROM proceedings).

He, J., Simonin, O., 1994. Modélisation numérique des écoulements turbulents gaz–solides en conduite verticale. Collection des notes internes de la DER, Electricité de France.

Lorenz, A., Tuozzolo, C., Louge, M.Y., 1997. Measurements of impact properties of small, nearly spherical particles. Experimental Mechanics 37 (3), 292–298.

Lun, C.K.K., Savage, S.B., 1987. A simple kinetic theory for granular flow of rough, inelastic, spherical particles. J. Appl. Mech 54, 47–53.

Lun, C.K.K., Bent, A.A., 1994. Numerical simulation of inelastic frictional spheres in simple shear flow. J. Fluid Mech 258, 335–353.

Lun, C.K.K., Liu, H.S., 1997. Numerical simulation of dilute turbulent gas–solid flows in horizontal channels. Int. J. Multiphase Flow 23 (3), 575–605.

Matsumoto, S., Saito, S., 1970a. On the mechanism of suspension of particles in horizontal pneumatic conveying: Monte Carlo simulation based on the irregular bouncing model. J. Chem. Eng. Japan 3, 83–92.

Matsumoto, S., Saito, S., 1970b. Monte Carlo simulation of horizontal pneumatic conveying based on the rough wall model. J. Chem. Eng. Japan 3, 223–230.

Morsi, S.A., Alexander, A.J., 1972. An investigation of particle trajectories in two-phase flow systems. J. Fluid Mech 55, 193–208.

Oesterlé, B., Petitjean, A., 1991. Simulation of particle-to-particle interactions in gas–solid flows. In: Proc. 1st Int. Conf. Multiphase Flows (ICMF'91), Tsukuba, Japan, 1, 91–94.

Oesterlé, B., Petitjean, A., 1993. Simulation of particle-to-particle interactions in gas–solid flows. Int. J. Multiphase Flow 19 (1), 199–211.

Oesterlé, B., Bui Dinh, T., 1998. Experiments on the lift of a spinning sphere in a range of intermediate Reynolds numbers. Exp. in Fluids 25 (1), 16–22.

Ottjes, J.A., 1978. Digital simulation of pneumatic particle transport. Chem. Eng. Sci 33 (6), 783–786.

Schade, K.-P., Erdmann, H.-J., Petrak, D., 1996. Experimental investigation of the particle–wall collision under particular consideration of the wall roughness. In: Proc. ASME Summer Meeting, San Diego, CA, FED-Vol. 236, 759–766.

Schade, K.-P., Hådrich, Th., 1998. Investigation of influence of wall roughness on particle–wall collision. In: Proc. 3rd Int. Conf. on Multiphase Flow (ICMF'98), Lyon, France, Paper 250 (CD ROM proceedings).

Sommerfeld, M., 1992. Modelling of particle–wall collisions in confined gas-particle flows. Int. J. Multiphase Flow 18 (6), 905–926.

Sommerfeld, M., 1994. The importance of detailed measurements for the validation of numerical models and methods for dispersed two-phase flows. In: Celik, I., et al. (Eds.), Experimental and Computational Aspects of Validation of Multiphase Flow CFD Codes, ASME, Washington DC, FED-Vol. 180, pp. 1–14.

Tanaka, T., Tsuji, Y. 1991. Numerical simulation of gas–solid two-phase flow in a vertical pipe: on the effect of inter-particle collision. Gas–Solid Flows 1991, ASME/FED-Vol. 121, 123–128.

Tanaka, T., Kiribayashi, K., Tsuji, Y., 1991. Monte Carlo simulation of gas–solid flow in a vertical pipe or channel. In: Proc. Int. Conf. on Multiphase Flows '91, Tsukuba, Japan, 439–442.

Tsuji, Y., Oshima, T., Morikawa, Y., 1985. Numerical simulation of pneumatic conveying in a horizontal pipe. KONA 3, 38–51.

Tsuji, Y., Tanaka, T., Ishida, T., 1990. Graphic simulation of plug conveying. In: Proc. Pneumatech 4, Glasgow, Scotland, 39–50.

Walton, O.R., 1993. Numerical simulation of inelastic, frictional particle–particle interactions. In: Roco, M.C. (Ed.), Particulate Two-Phase Flow. Butterworth-Heinemann, Boston, pp. 884–911 chapt. 25.